



# Flexible scattering order formulation of the discrete dipole approximation

YNON HEFETS<sup>\*</sup> AND CARYNELISA HASPEL

Fredy and Nadine Herrmann Institute of Earth Sciences, The Hebrew University of Jerusalem, Jerusalem, Israel  
\*ynon.hefets@mail.huji.ac.il

Received 23 May 2023; accepted 4 July 2023; posted 10 July 2023; published 2 August 2023

The discrete dipole approximation (DDA) is a well-known method for computation of the scattering of light from nonspherical particles. Here, we present a new scattering order formulation (SOF) of the DDA that allows the user to represent the scattering particle with higher flexibility than in conventional DDAs, while the computer memory required always scales as  $O(N)$ . In our new SOF, the user can locate each dipole independently, or off-grid, in space, assign each dipole a unique size and a unique dipole shape as appropriate, and assign each dipole a unique magneto-electric polarizability with no constraints. The cost of this flexibility is that the computation time is increased from  $O(N \log N)$  to  $O(N^2)$ . To compensate, our model allows the user to vary the range of dipole interaction in a unique manner. We find that, in cases in which the scatterer has at least one dimension that is sufficiently small compared with the wavelength, a relatively small number of iterations is required for convergence of the simulation, and in addition, a small dipole interaction range can be invoked to reduce the computation time to  $O(N)$  while still producing results that are sufficiently accurate. © 2023 Optica Publishing Group

<https://doi.org/10.1364/AO.496245>

## 1. INTRODUCTION

The importance of accurately modeling the scattering of solar radiation by realistically shaped (i.e., nonspherical) aerosol and hydrosol particles is well established [1–4], with implications for improving estimates of climate forcing by aerosol particles [5,6], improving retrievals in remote sensing of atmospheric and marine environments [7–10], improving predictions of the propagation of linearly and circularly polarized light in environments containing polarization sensitive organisms [11,12], improving image processing in scattering environments [13,14], and improving algorithms for underwater communication and LiDAR applications [15,16].

The discrete dipole approximation (DDA), also known as the coupled dipole approximation, is a well-known method for calculating the scattering of light from nonspherical scattering particles [17–21]. In DDA simulations, the scattered particle is divided into a three-dimensional grid of polarized volume elements, each of which is small enough compared with the incident wavelength that it functions as an induced radiating dipole. The radiation radiated by a given dipole is dictated by the electric field of the incident wave and by the electric fields of the waves radiated from all of the other dipoles. The DDA has been demonstrated to be a robust method and has been implemented extensively to compute the scattering of light by many types of scatterers, including interstellar dust, nonspherical aerosol particles, and nonspherical hydrosol particles [4,17,18,22,23].

Conventional implementations of the DDA involve solving a system of coupled equations for the exciting electric field at the

center of each dipole simultaneously (see, e.g., [21]). Scattering order formulations (SOFs) of the DDA, on the other hand, are perturbative methods that follow the succession of radiative interactions (orders of scattering) among the dipoles [24–27]. In general, SOFs of the DDA present several advantages. By following the succession of radiative interactions among the dipoles, SOFs can provide additional physical insights into the process of scattering. Further, for certain extreme scatterer shapes, such as scatterers with long, narrow features, SOFs can converge to an accurate solution more readily than conventional DDA algorithms. (See, e.g., [26,27], and references therein.) On the other hand, the range of scatterer parameter space (size parameter, complex refractive index of the scatterer with respect to the surrounding medium) for which SOFs converge is generally smaller than with conventional DDAs [21].

In this study, we present a new SOF of the DDA with the aim of not only retaining the aforementioned advantages of the SOF approach but also adding new features that enhance the method's flexibility as well as its efficiency in certain cases. The new features are as follows. 1) While conventional DDA algorithms (as well as some SOFs) that employ fast-Fourier-transform (FFT) and conjugate-gradient (CG) methods require a regular grid in order to achieve a computation time of  $O(N \log N)$ , our direct SOF iterative procedure does not necessitate placing the dipoles on a regular grid. In our new SOF, the user can locate each dipole independently, or off-grid, in space. Here, we investigate extreme cases of off-grid locations, such as the “random” locations of the dipoles in an amorphous

material, in addition to cases with dipoles on a regular grid. 2) In conventional DDAs and SOFs, the computer memory required is generally  $O(N^2/n_x)$ , where  $n_x$  is the grid size along one of the dimensions, though this depends on the shape of the scatterer and the orientation of the scatterer relative to the incident electric field [21]. In our new SOF, on the other hand, the computer memory required scales as  $O(N)$  regardless of the shape of the scatterer, the orientation of the scatterer relative to the incident electric field, the size of the dipoles, the arrangement of the dipoles, or any other characteristic of the dipoles. This is true even in the case of aggregates and other porous scatterers; thus, our SOF can be particularly useful for such scatterers. 3) In our new SOF, the user can assign each dipole a unique size (but still small compared with the wavelength) and a unique dipole shape as appropriate. Thus, the user can optimize the resolution of the discretization of a scatterer that has fine features in its outer envelope and/or complicated internal inhomogeneities. Note that the fact that the user can assign each dipole a unique size is reminiscent of but not identical to adaptive discretization. In adaptive discretization, the sizes of the dipoles are varied as multiples of the lattice constant (see, e.g., [28]), whereas in our model, there is no need to use a regular grid at all. We note that the DDA model ADDA [29], as of Version 1.4, includes an option for rectangular (parallelepiped) dipoles, but the shape of the dipoles is identical throughout the scatterer; the choice of rectangular dipoles is used to accelerate the computation if at least one dimension of the scatterer is smaller than the wavelength and not to improve the resolution of the discretization of the scatterer [29,30]. 4) While conventional DDA algorithms that employ FFT and CG methods require that the polarizability be at most a symmetric tensor in order to achieve a computation time of  $O(N \log N)$ , in our new SOF, the user can assign each dipole a unique polarizability with no constraints. Each individual (magnetoelectric) polarizability tensor may be isotropic, anisotropic and symmetric or anisotropic and antisymmetric (see, e.g., [31] for a description of these forms of the polarizability), with no change in the computer memory required or in the computation time. This is an advantage for simulating scattering by scatterers with complicated internal chirality and/or birefringence features, in addition to possible complicated external and internal shape features. 5) Our new SOF allows the user to vary the range of dipole interaction with ease in a unique manner that differs from, e.g., the fast multipole method (FMM) [21,32,33] (see Section 2); we also explore the implications of varying the range of dipole interaction in this unique manner on the convergence, computation time, and accuracy of the SOF of the DDA.

In this study, we present a first examination of the capabilities of our new, flexible SOF framework. We simulate the scattering of light by scatterers with regular overall shapes (spherical and cylindrical), with dipoles arranged on a regular grid, with dipoles arranged in amorphous configurations, and with different ranges of dipole interaction. Although our SOF allows each dipole in the scatterer to have a unique size and unique isotropic or anisotropic polarizability, for simplicity, in this work, the dipoles of each scatterer have a uniform size and isotropic polarizability.

In Sections 3.A and 3.B, we verify the accuracy of our new SOF by comparing our simulations of scattering by overall

spherical scatterers to the exact solution for Mie scattering by a sphere [34] and to the output of the conventional DDA code ADDA [29]. In Section 3.C, we discuss the convergence tendency of our new SOF for different scatterers. In Section 3.D, we investigate the effect of varying the range of dipole interaction on the accuracy of the scattering calculations.

## 2. MODEL DESCRIPTION

In our SOF of the DDA, as in other DDA methods, we discretize a scattering particle into dipole-sized volume elements, each very small relative to the wavelength of the incident radiation. We assume that the electric field at the location of each dipole can be written as a perturbed field

$$\mathbf{E}(\mathbf{r}) = \mathbf{E}_0(\mathbf{r}) + \mathbf{E}_1(\mathbf{r}) + \mathbf{E}_2(\mathbf{r}) + \dots, \quad (1)$$

where  $\mathbf{E}_0(\mathbf{r}) \equiv \mathbf{E}_{\text{inc}}(\mathbf{r})$  is the incident electric field, and  $\mathbf{r}$  is the position vector relative to the origin. In Eq. (1),  $\mathbf{E}_1(\mathbf{r})$  is the scattered electric field following the interaction of the dipoles with the incident field,  $\mathbf{E}_2(\mathbf{r})$  is the scattered electric field following the interaction of the dipoles with  $\mathbf{E}_1(\mathbf{r})$ , and so forth. The dipole moment of a radiating dipole in the field given by Eq. (1) is

$$\begin{aligned} \mathbf{p}_l &= \varepsilon_m \boldsymbol{\alpha}_l \mathbf{E}(\mathbf{r}_l) \\ &= \varepsilon_m \boldsymbol{\alpha}_l \mathbf{E}_0(\mathbf{r}_l) + \varepsilon_m \boldsymbol{\alpha}_l \mathbf{E}_1(\mathbf{r}_l) + \varepsilon_m \boldsymbol{\alpha}_l \mathbf{E}_2(\mathbf{r}_l) + \dots \\ &= \mathbf{p}_{l,0} + \mathbf{p}_{l,1} + \mathbf{p}_{l,2} + \dots \end{aligned} \quad (2)$$

The  $n$ th order of the electric field,  $\mathbf{E}_n(\mathbf{r}_l)$ , at the location of dipole  $l$  due to dipole  $j$  is equal to

$$\begin{aligned} \mathbf{E}_n(\mathbf{r}_l) &= \sum_{j \neq l}^N \frac{\exp(ikr_{lj})k^3}{4\pi\varepsilon_m} \left\{ \left( \frac{1}{k^3 r_{lj}^3} - \frac{i}{k^2 r_{lj}^2} \right) \right. \\ &\quad \left. \left[ 3\hat{r}_{lj} \left( \hat{r}_{lj} \cdot \mathbf{p}_{n-1,j} \right) - \mathbf{p}_{n-1,j} \right] - \frac{1}{kr_{lj}} \hat{r}_{lj} \times \left( \hat{r}_{lj} \times \mathbf{p}_{n-1,j} \right) \right\}, \end{aligned} \quad (3)$$

where the sum is over  $N$  dipoles,  $r_{lj}$  is the distance between dipoles  $l$  and  $j$ ,  $r_{lj} = |\mathbf{r}_j - \mathbf{r}_l| \hat{r}_{lj} = \frac{\mathbf{r}_j - \mathbf{r}_l}{r_{lj}}$ , is the unit vector,  $k$  is the wavenumber, and  $i$  is the imaginary unit. In Eq. (2),  $\varepsilon_m$  is the dielectric constant of the surrounding medium,  $\varepsilon_m = \varepsilon_0 n_m^2$ , where  $\varepsilon_0$  is the vacuum permittivity, and  $n_m$  is the (real) refractive index of the surrounding medium. The polarizability tensor of the  $l$ th dipole is represented by  $\boldsymbol{\alpha}_l$  and includes the self “radiative reaction” correction [18,35,36],

$$\boldsymbol{\alpha}_l = \boldsymbol{\alpha}_{0,l} \left( \mathbb{I} - i \frac{k^3}{6\pi} \boldsymbol{\alpha}_{0,l} \right)^{-1}, \quad (4)$$

where  $\mathbb{I}$  is the unity matrix, and  $\boldsymbol{\alpha}_{0,l}$  is the uncorrected polarizability tensor

$$\boldsymbol{\alpha}_{0,l} = 3V_l(\boldsymbol{\epsilon}_{s,l} - \varepsilon_m \mathbb{I})(\boldsymbol{\epsilon}_{s,l} + 2\varepsilon_m \mathbb{I})^{-1}, \quad (5)$$

where  $\boldsymbol{\epsilon}_{s,l}$  is the dielectric tensor of the  $l$ th dipole of the scatterer, and  $V_l$  is the volume of a single dipole.

For a homogeneous and isotropic scattering particle,  $\alpha_{0,l} = \alpha_0$  is a scalar (i.e., via the Clausius–Mossotti relation); for a nonisotropic scattering particle,  $\alpha_{0,l}$  is a symmetric or antisymmetric tensor (or a combination of both), depending on whether the scattering particle material exhibits birefringence and/or optical activity [31].

After calculating the dipole moments to satisfactory accuracy, the total scattered field in the far field is evaluated by summing the far field contributions of all of the dipoles:

$$\mathbf{E}_{\text{sca}}(\mathbf{r}) = - \sum_{l=1}^N \frac{\exp[i\mathbf{k} \cdot (\mathbf{r} - \mathbf{r}_l)]k^2}{4\pi\epsilon_m|\mathbf{r}|} \hat{r} \times (\hat{r} \times \mathbf{p}_l), \quad (6)$$

In most DDA methods, the minimal size of a dipole is the grid constant of the computational grid; a rule of thumb often used to select the dipole size is that the width of a dipole should be less than or equal to approximately one-tenth the size that the wavelength would be inside of the particle material [20,21]. As mentioned in Section 1, in our new SOF, the dipole size is not constrained to be constant; thus, there is no fixed computational grid, and we can easily construct complex particles with small features and achieve high shape resolution.

The main disadvantage of the lack of a fixed computational grid and the freedom of the option to choose  $\alpha_{0,l}$  to be an anti-symmetric tensor is the lack of the ability to use FFT and CG methods. Therefore, the computation time of iteratively solving Eqs. (2) and (3) is  $O(N^2)$  rather than  $O(M\log N)$ . As mentioned in Section 1, to improve the computation time without a fixed grid, our new SOF provides the ability to vary the range of dipole interaction in a unique manner. To vary the range,  $R$ , of dipole interaction, the sum in Eq. (3) only includes the fields contributed by dipoles  $j$  whose distance from dipole  $l$  is less than or equal to  $R$ , i.e., the sum in Eq. (3) only includes dipoles for whom  $r_{lj} \leq R$ . The degree of coupling, i.e., what fraction of dipoles affect the field of a specific dipole, is varied from full coupling, in which all dipoles interact with all other dipoles, to weak coupling, in which the dipoles interact only with their near neighbors. Note that, as mentioned in Section 1, our method of restricting the range of dipole interaction is reminiscent of but not the same as the FMM. In the FMM, dipoles are grouped into hierarchies, and each hierarchical group works as a single unit. In the FMM, essentially, even a dipole on the edge of a given hierarchical group interacts with dipoles outside of the group in an identical way to every other dipole in the hierarchical group [21,32,33]. In our method, on the other hand, each dipole is the center of its own group and interacts with a different set of dipoles. We can think of our method as restricting the range of interaction by applying a Heaviside function to each dipole individually. For comparison, we also test zero-coupling, in which the electric dipole moments are affected only by the external incident field. Such zero-coupling is equivalent to the Rayleigh–Gans–Debye (RGD) approximation (see, e.g., [37]).

The computation of the extinction efficiency ( $Q_{\text{ext}}$ ) and absorption efficiency ( $Q_{\text{abs}}$ ) in our simulations is completed using the following equations, based on Eqs. (8) and (9) from [20]:

$$Q_{\text{ext}} = \frac{k}{A|\mathbf{E}_0|^2\epsilon_m} \sum_{l=1}^N \text{Im} [\mathbf{E}_0(\mathbf{r}_l)^* \cdot \mathbf{p}_l], \quad (7)$$

$$Q_{\text{abs}} = \frac{k}{A|\mathbf{E}_0|^2\epsilon_m} \sum_{l=1}^N \left\{ \text{Im}[\mathbf{p}_l \cdot \mathbf{E}(\mathbf{r}_l)^*] - \frac{k^3}{6\pi} \frac{|\mathbf{p}_l|^2}{4\pi\epsilon_m} \right\}, \quad (8)$$

where  $A$  is the geometrical cross-section of the scatterer. Though the scattering efficiency ( $Q_{\text{sca}}$ ) can be derived directly from the difference between the extinction efficiency and the absorption efficiency, i.e., via  $Q_{\text{sca}} = Q_{\text{ext}} - Q_{\text{abs}}$ , for higher accuracy [18,29], we derive the scattering efficiency directly from the calculated intensity according to Eq. (32) of [2]:

$$Q_{\text{sca}} = \frac{1}{A|\mathbf{E}_0|^2} \iint_{4\pi} |\mathbf{E}_{\text{sca}}(\mathbf{r})| r^2 d\Omega, \quad (9)$$

where the integration is over  $4\pi$  steradians of solid angle  $\Omega$  at a distance  $r$  from the center of the domain in the far-field regime of the scatterer.

### 3. SIMULATION RESULTS

In each scattering simulation, the wavelength of the incident light is taken to be  $\lambda_0 = 0.500 \mu\text{m}$  with respect to vacuum, and the incident light wave propagates along the  $z$  axis ( $\hat{k}_{\text{inc}} = \hat{z}$ ). The (real) refractive index of the surrounding medium is taken to be that of water,  $n_m = 1.335$  [38]; thus, the wavelength relative to the surrounding medium is, roughly,  $\lambda = 0.375 \mu\text{m}$ .

As mentioned in Section 1, for the sake of testing the effects of dipole shape and polarizability, dipole size, and the range of dipole interaction using our new SOF, we take the overall shape of the scatterer to be that of either a sphere or a cylinder. We construct the spherical scatterers with two different dipole configurations: 1) dipoles on a regular cubical grid and 2) dipoles in an ideal amorphous solid (IAS) configuration [39,40] (see Fig. 1). We construct the cylindrical scatterers with dipoles on a regular cubical grid, where the shape of the cylinder is one of three types: a rod ( $H \gg \lambda$ ,  $D \ll \lambda$ ), a disk ( $H \ll \lambda$ ,  $D \gg \lambda$ ), or a regular cylinder ( $H$ ,  $D > \lambda$ ), where  $H$  and  $D$  are the cylinder height and cylinder diameter, respectively. In addition, for the cylindrical scatterers, we test two different orientations of the cylinder axis ( $c$  axis): 1)  $c$  axis parallel to the incident wave vector,  $\hat{c} \parallel \hat{k}_{\text{inc}}$ , and 2)  $c$  axis parallel to the  $x$  axis and perpendicular to the incident wave vector,  $\hat{c} \perp \hat{k}_{\text{inc}}$ . (See Fig. 2.) The polarizabilities are set using Eq. (5) with  $\epsilon_{s,l} = n_s^2$  and  $\epsilon_m = n_m^2$ , where  $n_s$  is the complex refractive index of the scatterer with respect to vacuum, and the volume of a dipole is

$$V_l = \frac{V}{N}, \quad (10)$$

where  $V$  is the total volume of the scatterer.

In the simulations, the elements of the scattering matrix (also known as the Mueller matrix),  $M_{ij}$ , are calculated with no normalization, while the scattering phase function,  $P(\theta, \phi)$ , is calculated with normalization such that  $\oint P(\theta, \phi) \sin \theta d\theta d\phi = 4\pi$ . In the cases where the scatterer shape is invariant to rotation about the  $z$  axis (a spherical particle or a cylindrical particle aligned parallel to  $\hat{k}_{\text{inc}}$ ), the scattering matrix and the phase function should be functions of the scattering (zenith) angle,  $\theta_{\text{sca}}$ , only [34]. Nevertheless, due to the discretization of the dipoles, the calculated scattering matrix and the phase function exhibit

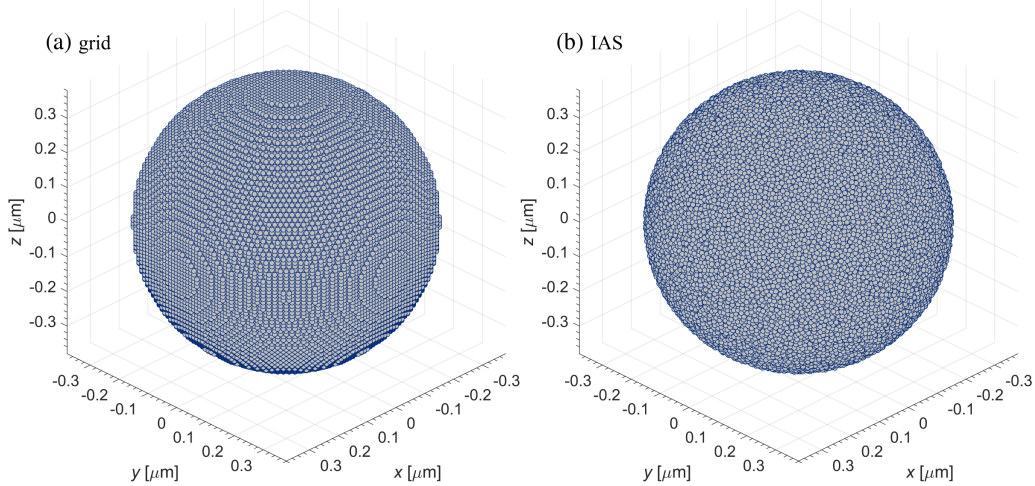


**Fig. 1.** Scatterer with an overall spherical shape with diameter 0.75  $\mu\text{m}$  and comprised of 221,119 dipoles. (a) Dipoles are located on a regular cubical grid with a lattice constant of 10 nm. (b) Dipoles are located in an IAS configuration [39,40] with an average distance of 10.5 nm between nearest neighbors. Note that, for the purposes of illustration, the dipole locations are indicated as small spheres, but the polarizability formulation is that of cubical dipoles with the dipole volume according to Eq. (10).

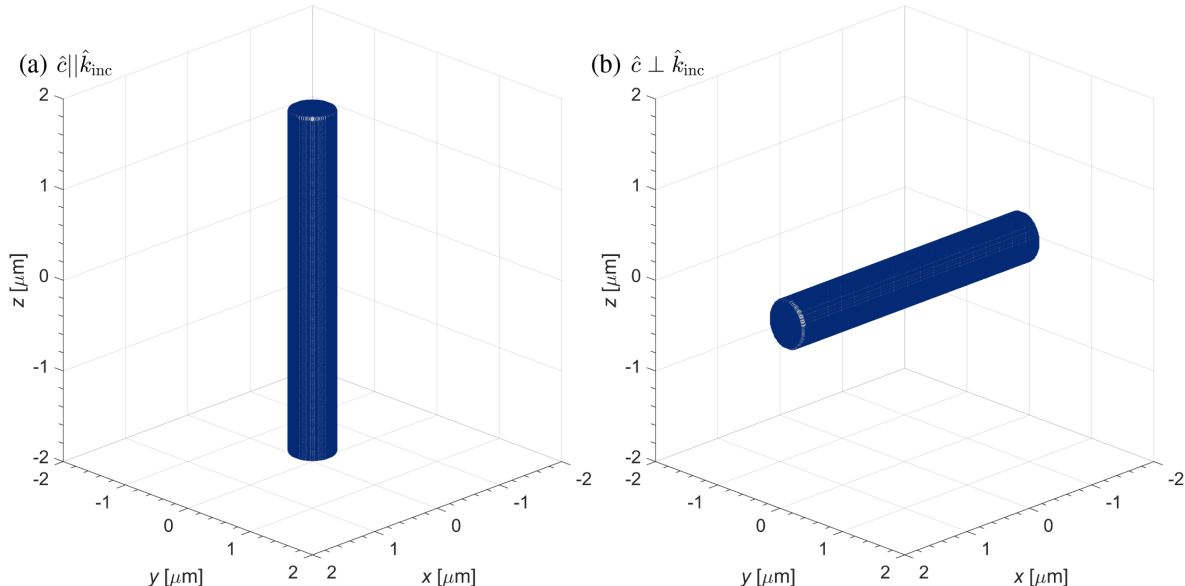


**Fig. 2.** Scatterer in the shape of a regular cylinder with a diameter of 0.49  $\mu\text{m}$  and a height of 3.75  $\mu\text{m}$  and comprised of 724,875 dipoles. (a) Cylinder is aligned parallel to  $\hat{k}_{\text{inc}}$ . (b) Cylinder is aligned perpendicular to  $\hat{k}_{\text{inc}}$ . Note that, for the purposes of illustration, the dipole locations are indicated as small spheres, but the polarizability formulation is that of cubical dipoles with the dipole volume according to Eq. (10).

a small variance with respect to the scattering azimuthal angle,  $\phi_{\text{sca}}$ ; therefore, we average the results for such cases over  $\phi_{\text{sca}}$ .

#### A. Comparison to Other Models

Here, we compare the output of our new SOF for a scatterer with an overall spherical shape against that of the conventional DDA code ADDA [29] (Version 1.2) and against a reference calculation obtained with the Mie scattering algorithm of Bohren and Huffman (BHMIE; [34]) translated into MATLAB by Boss [41]. The calculations of the elements of the scattering matrix as a function of scattering angle,  $M_{11}(\theta_{\text{sca}})$  and  $m_{ii}(\theta_{\text{sca}}) \equiv \frac{M_{ii}(\theta_{\text{sca}})}{M_{11}(\theta_{\text{sca}})}$ , for a scatterer with an

overall spherical shape and diameter  $D = 0.75 \mu\text{m}$  ( $\sim 2\lambda$ ) and a complex refractive index with respect to vacuum of  $n_s = 1.5 + i10^{-5}$  (the relative complex refractive index,  $m$ , is roughly  $1.12 + i7.49 \times 10^{-6}$ ) are shown in Figs. 3(a)–6(a). Given that there are only four independent elements in the scattering matrix of a sphere [34], only  $M_{11}$ ,  $m_{12}$ ,  $m_{33}$ , and  $m_{34}$  are presented. As mentioned above, in the SOF simulations, we employ two dipole configurations: 1) dipoles on a regular cubical grid and 2) dipoles in an IAS configuration [39,40]. Due to the fact that the IAS configuration is slightly more compact in space, in order to preserve the overall radius of the spherical particle, the dipole spacing (the width of a dipole) in the regular

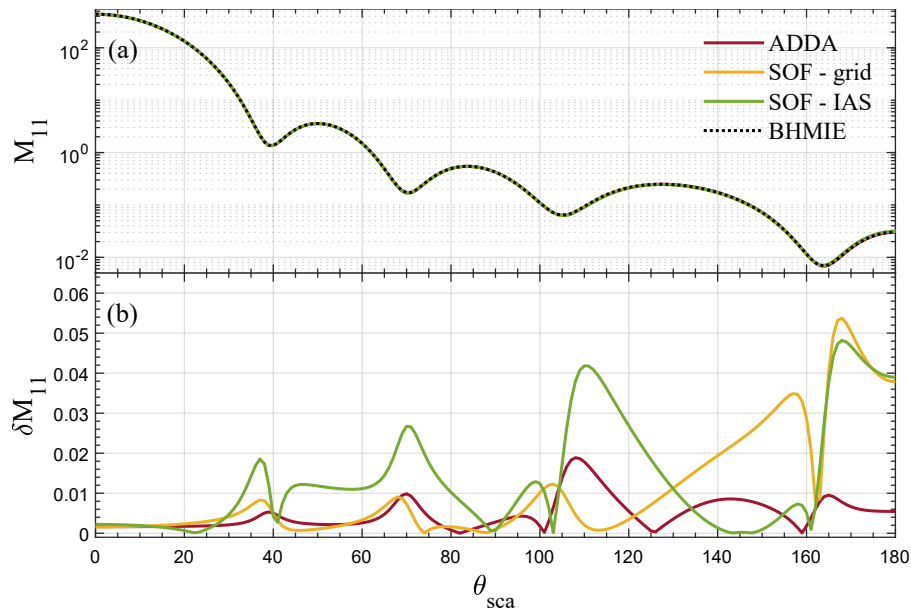


**Fig. 3.** (a) Scattering matrix element,  $M_{11}(\theta)$ , for scattering from a scatterer with an overall spherical shape with a diameter of  $0.75 \mu\text{m}$  and with a complex refractive index with respect to vacuum of  $n_s = 1.5 + i10^{-5}$ , with two different dipole configurations: regular cubical grid (yellow curve) and IAS (green curve). The results from ADDA [29] (red curve) and from BHMIE [34,41] (black dotted curve) are included for reference and comparison. The wavelength relative to the surrounding medium is  $0.3745 \mu\text{m}$ . (b)  $\delta M_{11}$  of the ADDA and the SOF calculations relative to the BHMIE solution.

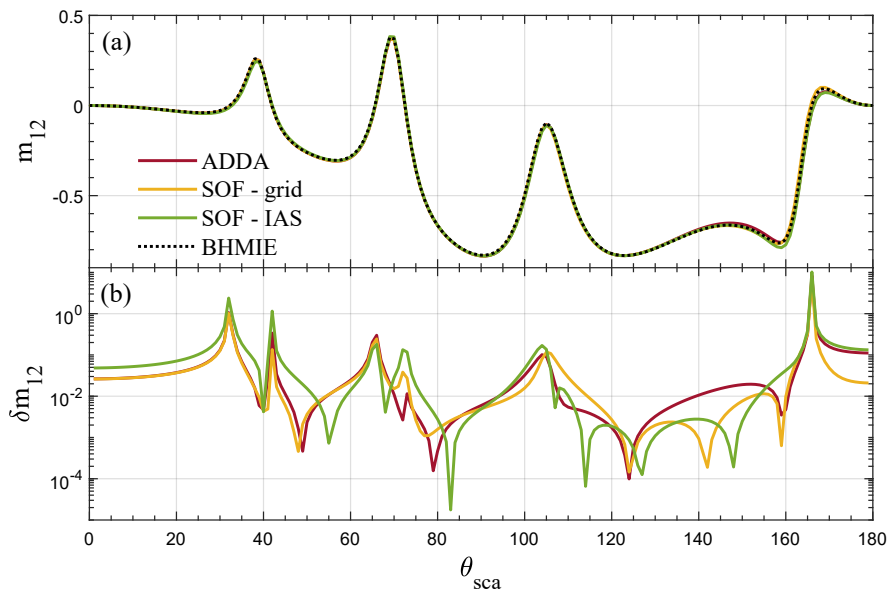


**Fig. 4.** (a) Scattering matrix element,  $m_{12}(\theta)$ , for scattering from a scatterer with an overall spherical shape with a diameter of  $0.75 \mu\text{m}$  and a complex refractive index with respect to vacuum of  $n_s = 1.5 + i10^{-5}$ , with two different dipole configurations: regular cubical grid (yellow curve) and IAS (green curve). The results from ADDA [29] (red curve) and from BHMIE [34,41] (black dotted curve) are for reference and comparison. The wavelength relative to the surrounding medium is  $0.3745 \mu\text{m}$ . (b)  $\delta m_{12}$  of the ADDA and the SOF calculations relative to the BHMIE solution.

cubical grid is set as 10 nm, while the width of a dipole in the IAS configuration is set as 10.5 nm. Both configurations contain 221,119 dipoles. Given that the IAS algorithm can produce different realizations for the same dipole size and dipole number, in order to guarantee that our results are not affected by a single configuration, we use the IAS algorithm to generate five different IAS realizations and average their scattering results.

For the sake of the comparison, in the ADDA simulations, the complex refractive index of the scatterer with respect to the surrounding medium, the dipole size, dipole shape, and polarizability formulation is identical to those in our new SOF simulations. We run the ADDA simulations using the following run options: `-lambda 374.531835206 -size 750.0 -m 1.1235955056 0.0000074906 -grid 75`

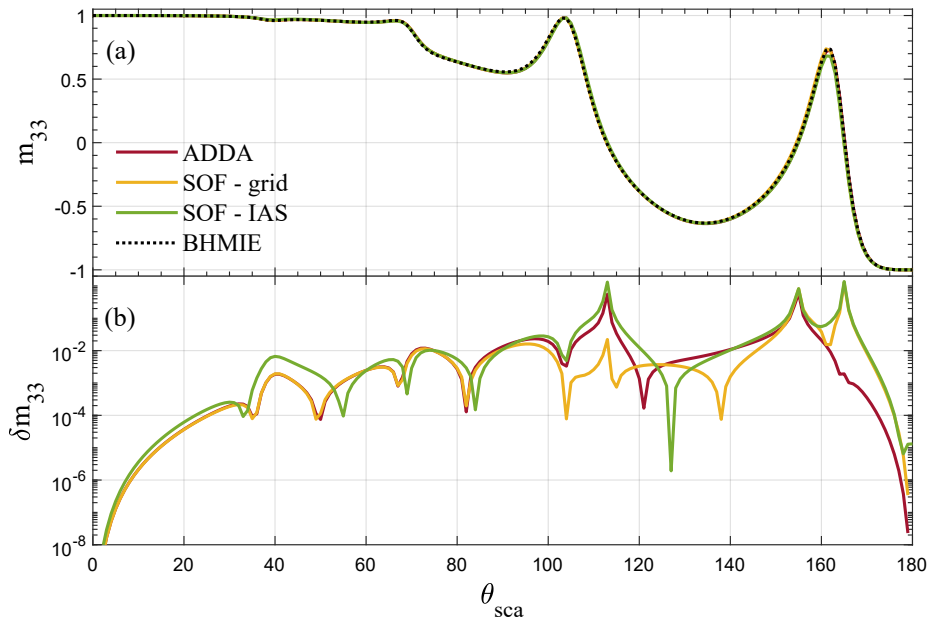


**Fig. 5.** (a) Scattering matrix element,  $m_{33}(\theta)$ , for scattering from a scatterer of overall spherical shape with a diameter of  $0.75 \mu\text{m}$  and a complex refractive index with respect to vacuum of  $n_s = 1.5 + i10^{-5}$ , with two different dipole configurations, regular cubical grid (yellow curve) and IAS (green curve). The results from ADDA [29] (red curve) and from BHMIE [34,41] (black dotted curve) are included for reference and comparison. The wavelength relative to the surrounding medium is  $0.3745 \mu\text{m}$ . (b)  $\delta m_{33}$  of the ADDA and the SOF calculations relative to the BHMIE solution.

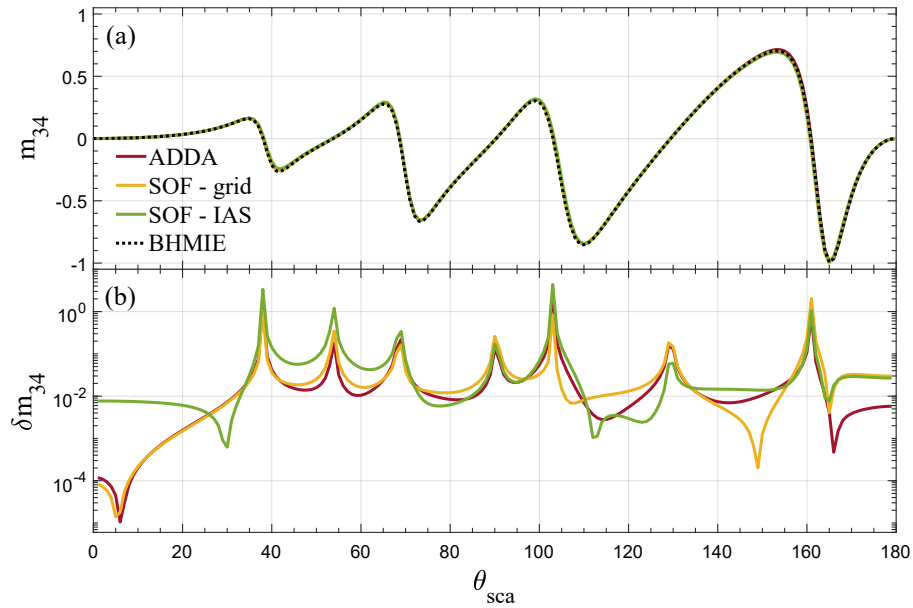


**Fig. 6.** (a) Scattering matrix element,  $m_{34}(\theta)$ , for scattering from a scatterer of overall spherical shape with a diameter of  $0.75 \mu\text{m}$  and a complex refractive index with respect to vacuum of  $n_s = 1.5 + i10^{-5}$ , with two different dipole configurations: regular cubical grid (yellow curve) and IAS (green curve). The results from ADDA [29] (red curve) and from BHMIE [34,41] (black dotted curve) are included for reference and comparison. The wavelength relative to the surrounding medium is  $0.3745 \mu\text{m}$ . (b)  $\delta m_{34}$  of the ADDA and the SOF calculations relative to the BHMIE solution.

-pol rrc. In addition, in the ADDA simulations, random orientation (-orient avg) is *not* used. Thus, the conditions of the ADDA simulations match the conditions of our SOF simulations.

The relative difference in the scattering matrix elements between the respective DDA simulation and BHMIE, i.e.,  $\delta M_{ii} = \frac{|M_{ii,\text{BHMIE}}(\theta_{\text{sca}}) - M_{ii,j}(\theta_{\text{sca}})|}{M_{ii,\text{BHMIE}}(\theta_{\text{sca}})}$ , where  $j$  stands for either

ADDA or SOF, is shown in Figs. 3(b)–6(b) as a function of scattering (zenith) angle. The weighted mean absolute percentage error (MAPE) of the DDA simulations relative to the BHMIE results, averaged over azimuthal scattering angle and summed over the scattering (zenith) angle, i.e.,

$$\text{MAPE}(M_{ii}) = \frac{\sum |M_{ii,\text{BHMIE}}(\theta_{\text{sca}}) - M_{ii,j}(\theta_{\text{sca}})|}{\sum M_{ii,\text{BHMIE}}(\theta_{\text{sca}})} \quad (11)$$

**Table 1.** Mean Absolute Percentage Error Corresponding to the Simulations Shown in Fig. 4–6

	MAPE ( $M_{11}$ ) [ $\times 10^{-3}$ ]	MAPE ( $m_{12}$ ) [ $\times 10^{-2}$ ]	MAPE ( $M_{33}$ ) [ $\times 10^{-3}$ ]	MAPE ( $M_{34}$ ) [ $\times 10^{-2}$ ]
ADDA	$1.70 \pm 0.003$	$3.0 \pm 1.0$	$1.71 \pm 0.002$	$0.57 \pm 0.14$
SOF, grid	$1.92 \pm 0.02$	$3.0 \pm 0.8$	$1.93 \pm 0.02$	$0.60 \pm 0.09$
SOF, IAS	$2.00 \pm 0.08$	$6.3 \pm 0.2$	$2.00 \pm 0.08$	$1.60 \pm 0.20$

**Table 2.** Scattering, Absorption, and Extinction Efficiencies Corresponding to the Simulations Shown in Figs. 4–6

	$Q_{\text{sca}}$	$Q_{\text{abs}}$	$Q_{\text{ext}}$	$\Delta Q_{\text{ext}, \text{BHMIE}}$
BHMIE <sup>a</sup>	1.1214	$1.53 \times 10^{-4}$	1.1215	—
ADDA <sup>a</sup>	1.1194	$1.52 \times 10^{-4}$	1.1196	$1.7 \times 10^{-3}$
SOF, grid	1.1191	$1.40 \times 10^{-4}$	1.1191	$2.2 \times 10^{-3}$
SOF, IAS <sup>b</sup>	$1.1200 \pm 2.5 \times 10^{-4}$	$1.40 \times 10^{-4} \pm 10^{-8}$	$1.1200 \pm 2.4 \times 10^{-4}$	$1.3 \times 10^{-3} \pm 2.1 \times 10^{-4}$

<sup>a</sup>The BHMIE output includes only  $Q_{\text{ext}}$  and  $Q_{\text{sca}}$ ; the output of ADDA includes only  $Q_{\text{ext}}$  and  $Q_{\text{abs}}$ . The missing value for each, was calculated from the relationship  $Q_{\text{ext}} = Q_{\text{abs}} + Q_{\text{sca}}$ .

<sup>b</sup>The IAS results are averaged over the five different IAS realizations.

is given in Table 1. The calculated values of scattering, absorption, and extinction efficiency and the error in the calculated value of extinction efficiency for our SOF and for ADDA relative to BHMIE,  $\Delta Q_{\text{ext}, \text{BHMIE}} = \frac{|Q_{\text{ext}} - Q_{\text{ext}, \text{BHMIE}}|}{Q_{\text{ext}, \text{BHMIE}}}$ , are given in Table 2.

From Figs. 3–6 and Tables 1 and 2, we can see that, with these parameter sets, our new SOF simulations with both dipole configurations produces results that are in good agreement with ADDA and with BHMIE. [Note that, in Fig. 3(b), the scale of the  $y$  axes is linear; in Figs. 4(b)–6(b), the scale of the  $y$  axes is logarithmic.] The small differences from BHMIE are similar to those produced by DDA models in general when using a similar dipole resolution and polarizability formulation [19–21]. Interestingly, from Table 1, the simulations using ADDA and using our new SOF with the regular cubical grid dipole configuration produce scattering matrix elements that are closer to those of BHMIE than the simulation using our new SOF with the IAS dipole configuration, while conversely, from Table 2, the simulation using our new SOF with the IAS dipole configuration produces calculated efficiencies that are slightly closer to those of BHMIE than the simulations using ADDA or using our new SOF with the regular cubical grid dipole configuration.

## B. Variation of the Overall Scatterer Shape and Convergence of the Simulations

As mentioned in Section 1 and as discussed in [21,25–27], SOFs do not always converge, particularly when the scatterer is large with respect to the wavelength and compact (i.e., not porous, thin, or lacy). Here, we inspect the convergence tendency of our new SOF by tracking the value of the average relative error of the increment to the dipole moment,  $\Delta p = \frac{1}{N} \sum_l \frac{|p_{l,n-1} - p_{l,n}|}{p_0}$ , as a function of the order of scattering [i.e., as a function of the iteration number,  $n$ , or the number of terms taken in Eqs. (1) and (2)] for different overall scatterer shapes: a sphere with diameter  $D = 0.75 \mu\text{m}$  comprised of 221,119 dipoles on a regular cubical grid, as in the previous section; a disk with dimensions  $H = 0.05 \mu\text{m}$  and  $D = 4.29 \mu\text{m}$  comprised of 724,865 dipoles on a regular cubical grid; a rod with dimensions  $H = 195.9 \mu\text{m}$  and  $D = 0.07 \mu\text{m}$  comprised of 724,867

dipoles on a regular cubical grid; and a regular cylinder with dimensions  $H = 3.75 \mu\text{m}$  and  $D = 0.49 \mu\text{m}$  comprised of 724,875 dipoles on a regular cubical grid. We also inspect the convergence tendency as a function of the complex refractive index of the scatterer by varying the values of the real part of the refractive index of the scatterer,  $n_{s,r}$ , and the values of the imaginary part of the refractive index of the scatterer,  $n_{s,i}$ , respectively. The results are shown in Figs. 7–9.

In Fig. 7, the values of  $\Delta p$  of the dipoles of the overall spherical scatterer as a function of the iteration number is shown for different values of  $n_{s,r}$  ranging from 1.3 to 1.6 (i.e., the real part of the refractive index of the scatterer relative to the surrounding medium,  $m_{s,r}$ , ranges from roughly 0.97 to roughly 1.2). The simulation is set to stop if  $\Delta p \leq 10^{-6}$  or after 120 iterations, whichever comes first. We find that simulating scattering by a moderately large sphere with our current new SOF is more successful than simulating scattering by a moderately large sphere with the SOF presented in [26], albeit the current SOF simulation is with a different complex refractive index that includes mild absorption. On the other hand, the simulation for  $n_{s,r} = 1.75$  ( $m_{s,r} \cong 1.31$ ) strongly diverges, with  $\Delta p$  reaching a value greater than  $10^{10}$  after 60 iterations.

In Fig. 8(a), we present a comparison between the number of iterations required for the simulation to converge as a function of  $n_{s,r}$  (as in Fig. 7) and the MAPE( $M_{11}$ ) from the same simulation. The MAPE( $M_{11}$ ) for  $n_{s,r} = 1.588$  and for  $n_{s,r} = 1.6$  are superimposed on the same graph (green data points), even though their simulations reached 120 iterations before attaining a value of  $\Delta p \leq 10^{-6}$ . In Fig. 8(b), we present a similar comparison, but as a function of  $n_{s,i}$  in the range  $10^{-5}$  to  $10^{-1}$  (i.e., the imaginary part of the refractive index of the scatterer relative to the surrounding medium,  $m_{s,i}$ , ranges from  $7.5 \times 10^{-6}$  to  $7.5 \times 10^{-2}$ ). Interestingly, from Fig. 8(a), the MAPE( $M_{11}$ ) value does not increase monotonically with the magnitude of the refractive index, and its relative error even decreases as the magnitude of the refractive index increases, which might be due to the higher number of iterations that are necessary to achieve  $\Delta p \leq 10^{-6}$  in the case of the higher magnitude of the refractive index, which leads to better accuracy in the final values.

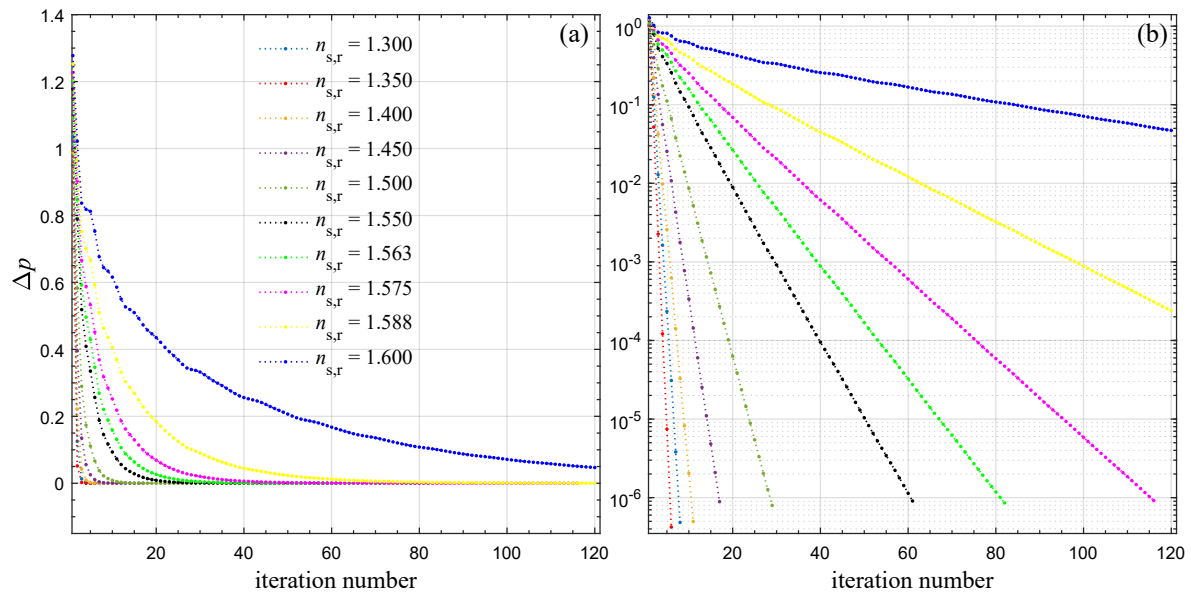


**Fig. 7.** Average relative error of the increment to the dipole moment,  $\Delta p$ , as function of iteration number in the calculations of scattering by a scatterer of overall spherical shape with different values of the real part of the refractive index with respect to vacuum, where the imaginary part of the refractive index with respect to vacuum is  $n_{s,i} = 10^{-5}$ : (a) linear scale; (b) logarithmic scale.

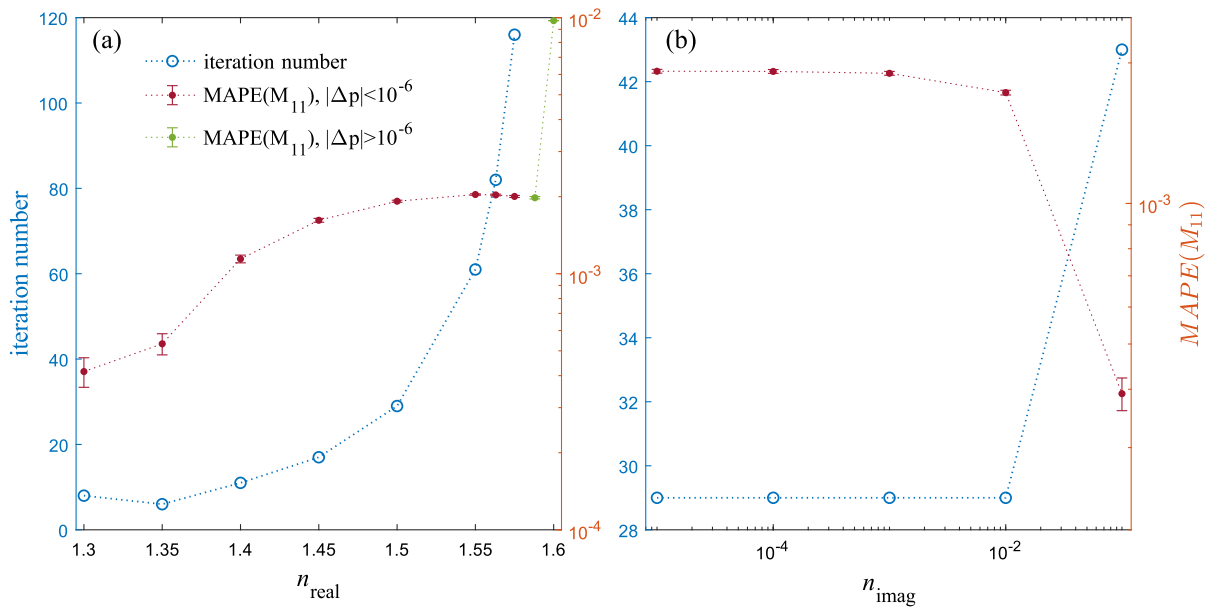


**Fig. 8.** Number of iterations of calculations required to achieve  $\Delta p \leq 10^{-6}$  and the corresponding MAPE of  $M_{11}$  (a) as a function of the real part of the complex refractive index with respect to the vacuum, where the imaginary part of the refractive index with respect to vacuum is  $n_{s,i} = 10^{-5}$ , and (b) as function of the imaginary part of the refractive index with respect to the vacuum, where the real part of the refractive index with respect to vacuum is  $n_{s,r} = 1.5$ . The green data points in (a) are the MAPE of  $M_{11}$  from simulations that do not achieve a value of  $\Delta p \leq 10^{-6}$  within 120 iterations.

In Fig. 9, the rate of convergence of the simulations of scattering by scatterers of overall disk, rod, or regular cylinder shape is shown. In the simulations of scattering by the disk and the rod, the complex refractive index is taken to be  $n_s = 1.5 + i10^{-5}$  with respect to vacuum. In the simulations of scattering by the regular cylinder, given that the simulation diverges for  $n_s = 1.5 + i10^{-5}$ , we test three other complex refractive indices with respect to vacuum,  $n_s = 1.35 + i10^{-5}$ ,  $n_s = 1.4 + i10^{-5}$ ,

and  $n_s = 1.45 + i10^{-5}$ . From Fig. 9, we find that the simulations of scattering by rods converge faster than the simulations of scattering by disks, while both converge much faster (achieve  $\Delta p \leq 10^{-6}$  after 8 to 13 iterations, respectively) than the simulations of scattering by a sphere with the same complex refractive index (which achieve  $\Delta p \leq 10^{-6}$  after 29 iterations), even though the rod and the disk each have a total volume that is  $\sim 3.5$  higher than that of the sphere.

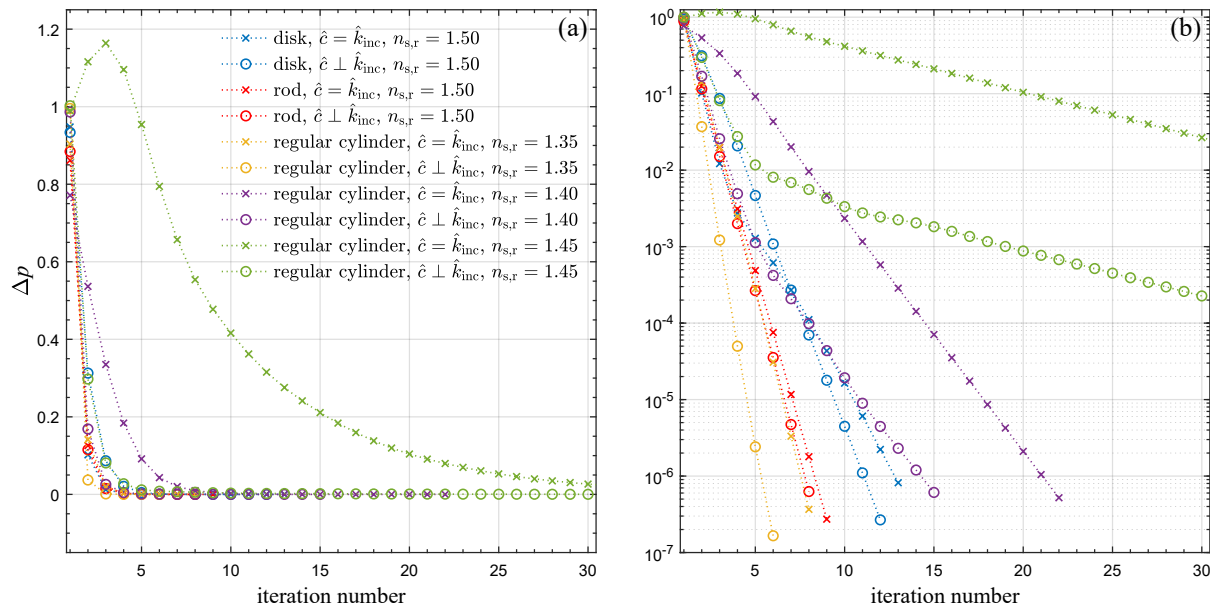


**Fig. 9.** Average relative error of the increment to the dipole moment,  $\Delta p$ , as function of iteration number in the calculations of scattering by scatterers of overall cylindrical shape with different orientations and/or different values of the real part of the refractive index with respect to vacuum, where the imaginary part of the refractive index with respect to vacuum is  $n_{s,i} = 10^{-5}$ : (a) linear scale; (b) logarithmic scale.

We also see from Fig. 9 that the orientation of the cylinder relative to the incident wave vector can have a major effect on the convergence of the simulation. For example, when the cylinder axis is perpendicular to  $\hat{k}_{\text{inc}}$ , the simulation converges faster as compared with the case when the cylinder axis is parallel to  $\hat{k}_{\text{inc}}$ . For a rod or disk, the simulation converges one iteration sooner (the computation is roughly 8%–11% faster) when the cylinder axis is perpendicular to  $\hat{k}_{\text{inc}}$  than when the cylinder axis is parallel to  $\hat{k}_{\text{inc}}$ . For a regular cylinder with a complex refractive index with respect to vacuum of  $n_s = 1.35 + i10^{-5}$ , the simulation converges two iterations sooner (the computation is  $\sim 22\%$  faster) when the cylinder axis is perpendicular to  $\hat{k}_{\text{inc}}$  than when the cylinder axis is parallel to  $\hat{k}_{\text{inc}}$ . For a regular cylinder with a complex refractive index with respect to vacuum of  $n_s = 1.4 + i10^{-5}$ , the simulation converges seven iterations sooner (the computation is  $\sim 32\%$  faster) when the cylinder axis is perpendicular to  $\hat{k}_{\text{inc}}$  than when the cylinder axis is parallel to  $\hat{k}_{\text{inc}}$ .

### C. Variation of the Range of Dipole Interaction

The scattering phase function,  $P(\theta, \phi)$ , of light scattered by scatterers with an overall rod, disk, regular cylinder, or spherical shape, respectively, and with varying ranges of dipole interaction (varying degrees of dipole coupling), is shown in Figs. 10–12. In each graph, the range of dipole interaction varies from no dipole-dipole interaction (zero-coupling), in which the electric dipole moments are affected only by the external incident field, to interaction between near neighbors only (weak coupling), to interaction with dipoles within a range of  $\lambda/4$  ( $\sim 0.094 \mu\text{m}$ ) only, to interaction with dipoles within a range of  $\lambda/2$  ( $\sim 0.187 \mu\text{m}$ ) only, to full interaction between all dipoles (full coupling). The MAPE of the scattering phase function

with limited dipole-dipole interaction relative to full coupling is given in Table 3.

From Fig. 10, we see that, apart from some local minimum values, the results for scattering by a scatterer with an overall rod shape or overall disk shape with its  $c$  axis parallel to the incident wave vector are similar for all ranges of dipole interaction; the curves overlap to such an extent that it is difficult to distinguish them. From Fig. 11, we see that, likewise, the results for scattering by a scatterer with an overall rod shape with its  $c$  axis perpendicular to the incident wave vector are similar for all ranges of dipole interaction. Again, the curves overlap to such an extent that it is difficult to distinguish them. The results for scattering by a scatterer with an overall disk shape with its  $c$  axis perpendicular to the incident wave vector are similar between the partial dipole-dipole interaction and full coupling; in the backward scattering hemisphere, however, there is a gap between the local maxima of the scattering phase function curves.

From Table 3, the MAPE of the scatterer with overall rod shape is  $<4.05\%$  for the various ranges of dipole interaction. Thus, for a rod, even zero dipole-dipole interaction can be used, and the computation time can be reduced from  $O(N^2)$  to  $O(N)$ . Likewise, for a disk with its axis parallel to the incident wave vector, the MAPE is  $<1.14\%$  for the various ranges of dipole interaction; thus, even zero dipole-dipole interaction can be used, and the computation time can be reduced from  $O(N^2)$  to  $O(N)$ . However, when the disk axis is perpendicular to the incident wave vector, the MAPE reaches as high as 9.83%, and whether the use of partial coupling of the dipoles is possible depends on the desired accuracy/precision of the results.

Our finding that the results are similar for all ranges of dipole interaction for a rod and for a disk with its axis parallel to the incident wave vector agrees with the findings of [42], which pointed out that, in particular, the component of the internal

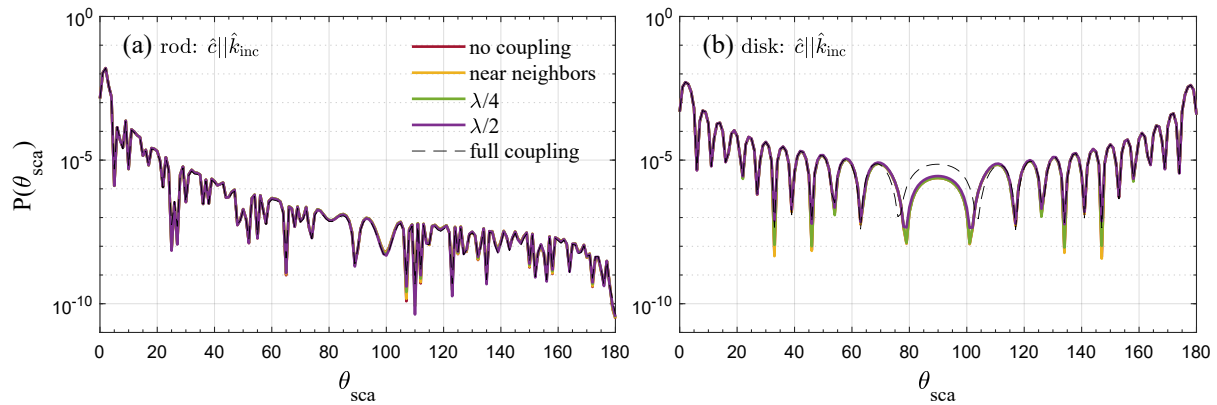


**Fig. 10.** Scattering phase function,  $P(\theta)$ , for unpolarized incident light as a function of scattering (zenith) angle as computed with our new SOF with different ranges of dipole interaction for a scatterer with an overall (a) rod shape or (b) disk shape oriented with its axis parallel to the incident wave vector. The complex refractive index of the scatterer with respect to vacuum is  $n_s = 1.5 + i10^{-5}$ .

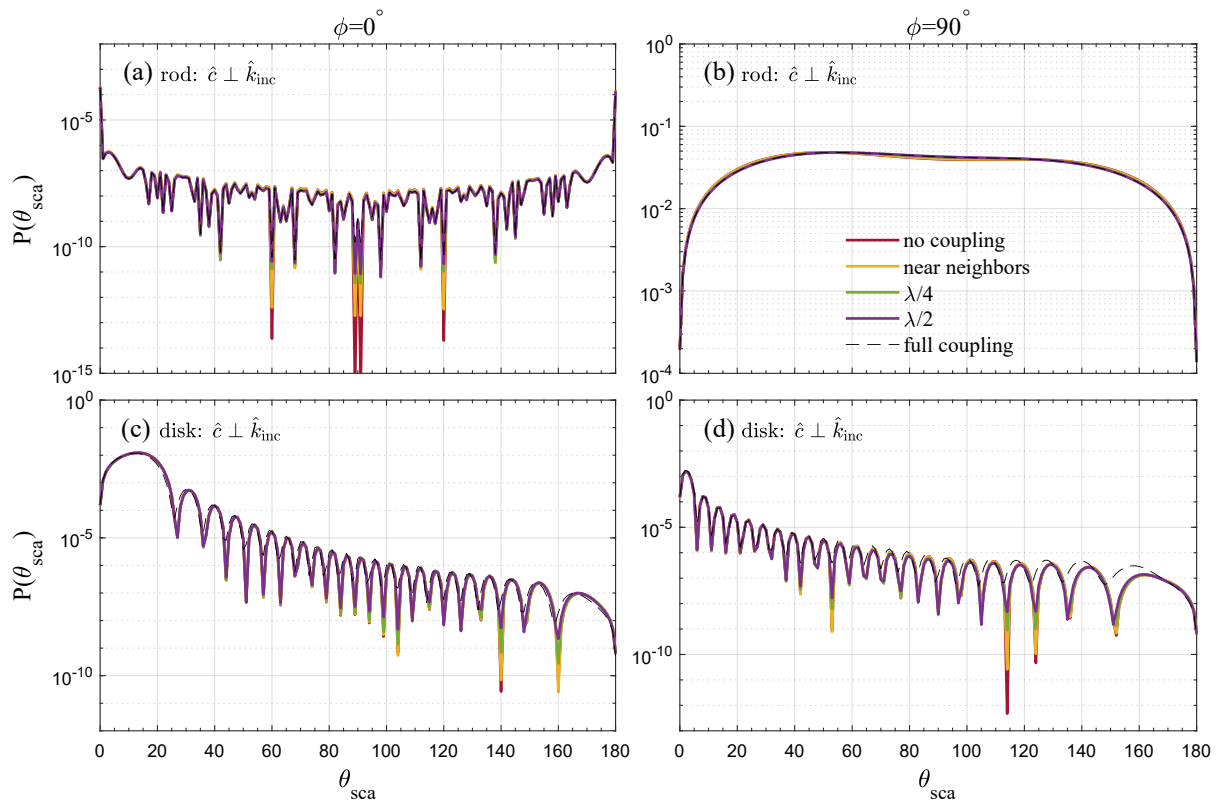


**Fig. 11.** Scattering phase function,  $P(\theta)$ , for unpolarized incident light as a function of scattering (zenith) angle as computed with our new SOF with different ranges of dipole interaction for a scatterer with an overall (a) (b) rod shape or (c) (d) disk shape oriented with its axis perpendicular to the incident wave vector. The complex refractive index of the scatterer with respect to vacuum is  $n_s = 1.5 + i10^{-5}$ . (a) and (c)  $\phi = 0^\circ$ , i.e., the scattering plane contains the axis of the cylinder. (b) and (d),  $\phi = 90^\circ$ , i.e., the scattering plane is perpendicular to the axis of the cylinder.

electric field that is perpendicular to the incident electric field can be calculated accurately with zero dipole-dipole interaction (i.e., with the RGD approximation) in the case of an aggregate of particles arranged in a plane perpendicular to the incident wave vector. This phenomenon also likely contributes to the fact that the SOF in general is known to converge well for scatterers that are narrow in at least one dimension. (See, e.g., the discussion in [26] and references therein.) In addition, as mentioned in Section 1, rectangular dipoles in conjunction with FFT and CG

methods can be used for accelerating the computation for such particles [29,30], with an improvement in computation time by up to a factor of 100. Another technique known as circulant preconditioning can also be used in conjunction with FFT and CG methods to accelerate the computation for such particles [43,44], with an improvement in computation time of up to a factor of 15. For comparison, with zero-coupling, we achieve an improvement in computation time by a factor of 100 for our

**Table 3.** Mean Absolute Percentage Error Corresponding to the Simulations Shown in Figs. 10–12

	No Coupling [ $\times 10^{-3}$ ]	Nearest Neighbors [ $\times 10^{-3}$ ]	$\frac{\lambda}{4}, \sim 0.094 \mu\text{m}$ [ $\times 10^{-3}$ ]	$\frac{\lambda}{2}, \sim 0.187 \mu\text{m}$ [ $\times 10^{-3}$ ]
Rod, $\hat{c} \parallel \hat{k}_{\text{inc}}$	7.2	7.2	7.2	7.1
Rod, $\hat{c} \perp \hat{k}_{\text{inc}}$	40.5	34.1	6.3	2.4
Disk, $\hat{c} \parallel \hat{k}_{\text{inc}}$	9.2	7.6	11.4	5.8
Disk, $\hat{c} \perp \hat{k}_{\text{inc}}$	78.8	79.0	80.9	80.5
Regular cylinder, $\hat{c} \parallel \hat{k}_{\text{inc}}$	97.7	97.7	98.3	97.5
Regular cylinder, $\hat{c} \perp \hat{k}_{\text{inc}}$	19.0	19.0	21.8	15.1
Sphere	79.2	79.4	85.3	65.9

disk-shaped scatterer and by a factor of 80 for our rod-shaped scatterer.

From Fig. 12 and from Table 3, we see that, for scattering by a regular cylindrical scatterer, as opposed to scattering by a rod- or disk-shaped scatterer, the limited dipole coupling provides a more accurate result, particularly in the direct forward scattering or direct backscattering directions, when the  $c$  axis is perpendicular to the incident wave vector. Our finding that limited dipole coupling can provide accurate results particularly in the direct backscattering direction agrees with the finding of Kahnert [45] that the backscattering cross section of an aggregate can be predicted accurately while limiting the interaction among the monomers of the aggregate.

For scattering from a spherical scatterer, except for a limited range of angles in the forward scattering direction, limiting the range of dipole interaction leads to an erroneous scattering phase function. [Note that, in the case of the spherical scatterer, there is almost no difference between zero-coupling and weak coupling; in Fig. 12(b), the red and yellow curves overlap to such an extent that it is difficult to distinguish them.]

#### 4. SUMMARY AND CONCLUSIONS

We developed a new SOF of the DDA that is flexible and allows the user to place dipoles of any size anywhere in the domain and to assign each dipole an individual polarizability tensor of any kind. Our new SOF also allows the user to control the range

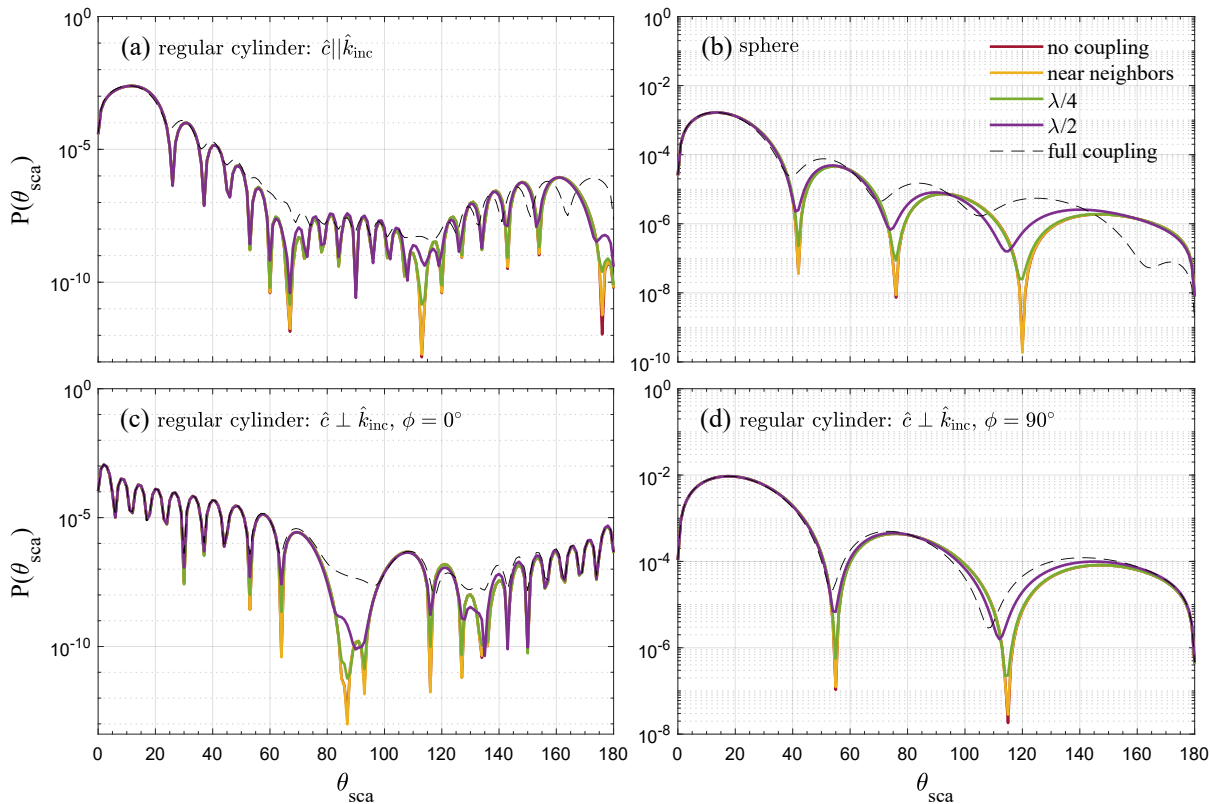


**Fig. 12.** Scattering phase function,  $P(\theta)$ , for unpolarized incident light as a function of scattering angle as computed with our new SOF with different ranges of dipole interaction for a scatterer with an overall (a) (c) (d) regular cylinder shape or (b) spherical shape. The complex refractive index of the scatterer with respect to vacuum is  $n_s = 1.4 + i10^{-5}$  for the cylinder and  $n_s = 1.5 + i10^{-5}$  for the sphere. (a)  $c$  axis is parallel to the incident wave vector, while in (c, d), the  $c$  axis is perpendicular to the incident wave vector. (c)  $\phi = 0^\circ$ , i.e., the scattering plane contains the axis of the cylinder. (d)  $\phi = 90^\circ$ , i.e., the scattering plane is perpendicular to the axis of the cylinder.

of dipole interaction in a unique manner. We validated our new SOF by comparing calculations of scattering of polarized light by a scatterer with an overall spherical shape using our new SOF to calculations with ADDA and with BHMIE, where the dipoles in our new SOF were arranged in either a cubical grid configuration or an ideal amorphous solid configuration. We found that ADDA and our new SOF match BHMIE to a similar extent. In addition, we found that the scattering phase function calculated with our new SOF lies slightly closer to the BHMIE curve when the dipoles are arranged in a regular grid configuration than when the dipoles are arranged in an IAS configuration. However, interestingly, the opposite is true regarding the scattering and extinction efficiencies. The efficiencies calculated with our new SOF are slightly closer to those calculated using BHMIE when the dipoles are arranged in an IAS configuration than when the dipoles are arranged in a regular grid configuration. This latter property may be useful in future calculations for cases in which the scattering/absorption/extinction efficiencies are the desired output.

We examined the convergence tendency of our calculations for scattering by scatterers of overall spherical and cylindrical shapes. We found that, for a scatterer with an overall spherical shape, the convergence of the calculations with a converge criterion of a precision of  $10^{-6}$  in  $\Delta p$  is strongly dependent on the relative complex refractive index. As the real part of the complex refractive index increases, the number of iterations necessary for convergence also increases. However, interestingly, the MAPE relative to BHMIE has a local maximum at  $n_{s,\text{real}} = 1.55$  with respect to vacuum, and the variance of the MAPE with respect to the scattering azimuthal angle (where the variance of the MAPE would be zero for a perfectly homogeneous spherical scatterer) even decreases with  $n_{s,\text{real}}$ . A possible explanation for this is that the higher number of iterations leads to better accuracy in the final values. We found that the convergence of calculations of scattering from a cylindrical scatterer depends on the aspect ratio of the cylinder and its orientation relative to the incident wave vector. The calculations for scattering by a rod with complex refractive index  $n_s = 1.5 + i10^{-5}$  with respect to vacuum converged after fewer than nine iterations, while the calculations for scattering by a disk with the same complex refractive index converged within 13 iterations. For comparison, the calculations of scattering from a sphere with the same complex refractive index took 29 iterations to converge, even though the volume of the rod and volume of the disk are each about three times higher than the volume of the sphere, and the calculations of scattering from a regular cylinder with a similar volume to the rod and disk only converged when the complex refractive index was reduced.

We investigated the effect of varying the range of dipole interaction (varying the degree of dipole coupling) in a unique manner that can be thought of as applying a Heaviside function to each dipole individually. We found that, for a scatterer with an overall spherical shape, only full dipole coupling produces sufficiently accurate results. For a rod or for a disk whose axis is parallel to the incident wave vector, however, even zero-coupling produces reasonably accurate results, and the computation time can be reduced from  $O(N^2)$  to  $O(N)$  accordingly. For a disk whose axis is perpendicular to the incident wave vector, the use of partial coupling of the dipoles may be possible, depending on the desired accuracy/precision of the results, but for the

most accurate results, full coupling should be used, and the computation time remains  $O(N^2)$ .

In summary, we find that our new, flexible SOF of the DDA presents a number of advantages. 1) The computer memory required scales as  $O(N)$  regardless of the shape of the scatterer, the orientation of the scatterer relative to the incident electric field, size of the dipoles, arrangement of the dipoles, or any other characteristic of the dipoles. This is true even in the case of aggregates and other porous scatterers; thus, our SOF can be particularly useful for such scatterers. 2) The fact that the model does not constrain the user to arrange the dipoles on a regular grid allows the user to build more precise scatterer shapes and to achieve more accurate simulations of scattering in some circumstances, e.g., by locating the dipoles in a more random configuration within the scatterer. 3) The fact that the model allows the user to vary the range of dipole interaction in a unique manner allows the user to reduce the computation time from  $O(N^2)$  to  $O(N)$  for scatterers with at least one dimension that is small compared with the wavelength of the incident radiation. In fact, for scatterers with at least one dimension that is small compared with the wavelength of the incident radiation, the number of iterations required to achieve convergence is relatively small even without varying the range of dipole interaction. Thus, the model should be particularly useful for such scatterers. This would also likely be an additional advantage when simulating aggregates and other porous scatterers. 4) The fact that each individual (magnetoelectric) polarizability tensor may be isotropic, anisotropic and symmetric, or anisotropic and antisymmetric with no change in the computer memory required or in the computation time is an advantage for simulating scattering by scatterers with complicated internal chirality and/or birefringence features. The performance of the model with dipoles with anisotropic polarizabilities will be examined in a future study.

**Funding.** Israel Science Foundation (2187/21).

**Acknowledgment.** The authors thank D. Strasser, who asked about the dipole interaction range, which gave us the idea to conduct the simulations as a function of dipole interaction range in this study. The authors also thank four anonymous reviewers of the original submission of this paper and the anonymous reviewer of the revision of the paper for their thorough and constructive comments.

**Disclosures.** The authors declare no conflicts of interest.

**Data availability.** The SOF model and the output shown in this study can be obtained from the authors by request.

## REFERENCES

1. M. I. Mishchenko, L. D. Travis, R. A. Kahn, and R. A. West, "Modeling phase functions for dust like tropospheric aerosols using a shape mixture of randomly oriented polydisperse spheroids," *J. Geophys. Res.* **102**, 16831–16847 (1997).
2. M. I. Mishchenko, J. W. Hovenier, and L. D. Travis, *Light Scattering by Nonspherical Particles: Theory, Measurements, and Applications* (Academic, 2000).
3. M. Kahnert, "Numerical solutions of the macroscopic Maxwell equations for scattering by non-spherical particles: a tutorial review," *J. Quant. Spectrosc. Radiat. Transfer* **178**, 22–37 (2016).
4. T. Nousiainen, E. Zubko, H. Lindqvist, M. Kahnert, and J. Tyynelä, "Comparison of scattering by different nonspherical, wavelength-scale particles," *J. Quant. Spectrosc. Radiat. Transfer* **113**, 2391–2405 (2012).

5. P. Forster, T. Storelvmo, K. Armour, W. Collins, J. L. Dufresne, D. Frame, D. J. Lunt, T. Mauritsen, M. D. Palmer, M. Watanabe, M. Wild, and H. Zhang, "2021: the Earth's energy budget, climate feedbacks, and climate sensitivity," in *Climate Change 2021: The Physical Science Basis. Contribution of Working Group I to the Sixth Assessment Report of the Intergovernmental Panel on Climate Change (IPCC)* (Cambridge University, 2021), pp. 923–1054.
6. K. S. Carslaw, L. A. Lee, C. L. Reddington, K. J. Pringle, A. Rap, P. M. Forster, G. W. Mann, D. V. Spracklen, M. T. Woodhouse, L. A. Regayre, and J. R. Pierce, "Large contribution of natural aerosols to uncertainty in indirect forcing," *Nature* **503**, 67–71 (2013).
7. O. Dubovik, Z. Li, M. I. Mishchenko, et al., "Polarimetric remote sensing of atmospheric aerosols: Instruments, methodologies, results, and perspectives," *J. Quant. Spectrosc. Radiat. Transfer* **224**, 474–511 (2019).
8. D. Koestner, D. Stramski, and R. A. Reynolds, "Characterization of suspended particulate matter in contrasting coastal marine environments with angle-resolved polarized light scattering measurements," *Appl. Opt.* **60**, 11161–11179 (2021).
9. M. Tzabari, W. Lin, A. Lerner, D. Iluz, and C. Haspel, "Sensitivity study on the contribution of scattering by randomly oriented nonspherical hydrosols to linear polarization in clear to semi-turbid shallow waters," *Appl. Opt.* **58**, 7258–7279 (2019).
10. J. D. van der Laan, J. B. Wright, D. A. Scrymgeour, S. A. Kemme, and E. L. Dereniak, "Evolution of circular and linear polarization in scattering environments," *Opt. Express* **23**, 31874–31888 (2015).
11. S. Sabbah, A. Lerner, C. Erlick, and N. Shashar, "Underwater polarization vision—a physical examination," in *Recent Research Developments in Experimental and Theoretical Biology* (2005), Vol. 1, 123–176.
12. N. Shashar, S. Johnsen, A. Lerner, S. Sabbah, C.-C. Chiao, L. M. Mäthger, and R. T. Hanlon, "Underwater linear polarization: physical limitations to biological functions," *Philos. Trans. R. Soc. B* **366**, 649–654 (2011).
13. J. S. Tyo, D. L. Goldstein, D. B. Chenault, and J. A. Shaw, "Review of passive imaging polarimetry for remote sensing applications," *Appl. Opt.* **45**, 5453–5469 (2006).
14. R. Wang, T. Ji, and G. Wang, "Haze removal by modeling the scattering properties of the medium," *IEEE Signal Process. Lett.* **27**, 1155–1159 (2020).
15. H. M. Oubei, C. Shen, A. Kamoun, E. Zedini, K.-H. Park, X. Sun, G. Liu, C. H. Kang, T. K. Ng, M.-S. Alouini, and B. S. Ooi, "Light based underwater wireless communications," *Jpn. J. Appl. Phys.* **57**, 08PA06 (2018).
16. D.-M. He and G. G. L. Seet, "Divergent-beam Lidar imaging in turbid water," *Opt. Laser. Eng.* **41**, 217–231 (2004).
17. E. M. Purcell and C. R. Pennypacker, "Scattering and absorption of light by nonspherical dielectric grains," *Astrophys. J.* **186**, 705–714 (1973).
18. B. T. Draine, "The discrete-dipole approximation and its application to interstellar graphite grains," *Astrophys. J.* **333**, 848–872 (1988).
19. J. J. Goodman, B. T. Draine, and P. J. Flatau, "Application of fast-Fourier-transform techniques to the discrete-dipole approximation," *Opt. Lett.* **16**, 1198–1200 (1991).
20. B. T. Draine and P. J. Flatau, "Discrete-dipole approximation for scattering calculations," *J. Opt. Soc. Am. A* **11**, 1491–1499 (1994).
21. M. A. Yurkin and A. G. Hoekstra, "The discrete dipole approximation: an overview and recent developments," *J. Quant. Spectrosc. Radiat. Transfer* **106**, 558–589 (2007).
22. C. F. Bohren and S. B. Singh, "Backscattering by nonspherical particles' a review of methods and suggested new approaches," *J. Geophys. Res.* **96**, 5269–5277 (1991).
23. C. Haspel and G. Adler, "The concept of apparent polarizability for calculating the extinction of electromagnetic radiation by porous aerosol particles," *J. Geophys. Res. Atmos.* **122**, 3944–3952 (2017).
24. P. Chiappetta, "Multiple scattering approach to light scattering by arbitrarily shaped particles," *J. Phys. A* **13**, 2101–2108 (1980).
25. S. B. Singh and C. F. Bohren, "Light scattering by an arbitrary particle: the scattering-order formulation of the coupled-dipole method," *J. Opt. Soc. Am. A* **5**, 1867–1872 (1988).
26. C. Haspel and M. Tzabari, "Sensitivity tests on the convergence tendency of the scattering order formulation of the discrete dipole approximation," *Appl. Opt.* **56**, 3547–3555 (2017).
27. C. Haspel and M. Sela, "Considerations concerning backscattering in the scattering order formulation of the discrete dipole approximation as applied to non-absorbing scatterers," *Appl. Opt.* **60**, 7664–7670 (2021).
28. C. Bourrelly, P. Chiappetta, T. J. Lemaire, and B. Torresani, "Multidipole formulation of the coupled dipole method for electromagnetic scattering by an arbitrary particle," *J. Opt. Soc. Am. A* **9**, 1336–1340 (1992).
29. M. A. Yurkin and A. G. Hoekstra, "The discrete-dipole-approximation code ADDA: capabilities and known limitations," *J. Quant. Spectrosc. Radiat. Transfer* **112**, 2234–2247 (2011).
30. D. A. Smirnov, P. C. Chaumet, and M. A. Yurkin, "Rectangular dipoles in the discrete dipole approximation," *J. Quant. Spectrosc. Radiat. Transfer* **156**, 67–79 (2015).
31. A. H. Sihvola, "Dielectric polarizability of a sphere with arbitrary anisotropy," *Opt. Lett.* **19**, 430–432 (1994).
32. N. Engheta, W. D. Murphy, V. Rokhlin, and M. S. Vassiliou, "The fast multipole method (FMM) for electromagnetic scattering problems," *IEEE Trans. Antennas Propag.* **40**, 634–641 (1992).
33. S. Jarvenpaa, J. Markkanen, and P. Yla-Oijala, "Broadband multilevel fast multipole algorithm for electric-magnetic current volume integral equation," *IEEE Trans. Antennas Propag.* **61**, 4393–4397 (2013).
34. C. F. Bohren and D. R. Huffman, *Absorption and Scattering of Light by Small Particles* (Wiley, 1983), pp. 477–482.
35. S. Albaladejo, R. Gómez-Medina, L. S. Froufe-Pérez, H. Marinchio, R. Carminati, J. F. Torrado, G. Armelles, A. García-Martín, and J. J. Sáenz, "Radiative corrections to the polarizability tensor of an electrically small anisotropic dielectric particle," *Opt. Express* **18**, 3556–3567 (2010).
36. A. Lakhtakia, "Strong and weak forms of the method of moments and the coupled dipole method for scattering of time-harmonic electromagnetic fields," *Int. J. Mod. Phys. C* **3**, 583–603 (1992).
37. C. M. Sorensen, "Light scattering by fractal aggregates: a review," *Aerosol Sci. Technol.* **35**, 648–687 (2001).
38. G. M. Hale and M. R. Querry, "Optical constants of water in the 200-nm to 200-μm wavelength region," *Appl. Opt.* **12**, 555–563 (1973).
39. L.-T. To, D. J. Daley, and Z. H. Stachurski, "On the definition of an ideal amorphous solid of uniform hard spheres," *Solid State Sci.* **8**, 868–879 (2006).
40. C.-Y. Lee, Z. H. Stachurski, and T. R. Welberry, "The geometry, topology and structure of amorphous solids," *Acta Mater.* **58**, 615–625 (2010).
41. E. Boss, *Adaptation of a Fortran Code of Bohren & Huffman to MATLAB* (University of MAINE, 1998).
42. A. E. Moskalensky, D. I. Strokotov, A. V. Chernyshev, V. P. Maltsev, and M. A. Yurkin, "Additivity of light-scattering patterns of aggregated biological particles," *J. Biomed. Opt.* **19**, 085004 (2014).
43. S. P. Groth, A. G. Polimeridis, A. Tambova, and J. K. White, "Circulant preconditioning in the volume integral equation method for silicon photonics," *J. Opt. Soc. Am. A* **36**, 1079–1088 (2019).
44. S. P. Groth, A. G. Polimeridis, and J. K. White, "Accelerating the discrete dipole approximation via circulant preconditioning," *J. Quant. Spectrosc. Radiat. Transfer* **240**, 106689 (2020).
45. M. Kahnert, "On the discrepancy between modeled and measured mass absorption cross sections of light absorbing carbon aerosols," *Aerosol Sci. Technol.* **44**, 453–460 (2010).